Chemical Engineering Journal 405 (2021) 126650

Contents lists available at ScienceDirect

Chemical Engineering Journal

journal homepage: www.elsevier.com/locate/cej

# Hierarchical core–shell $TiO_2$@LDH@$Ni(OH)_2$ architecture with regularly-oriented nanocatalyst shells: Towards improving the mechanical performance, flame retardancy and toxic smoke suppression of unsaturated polyester resin

Fukai Chu, Zhoumei Xu, Yifan Zhou, Shenghe Zhang, Xiaowei Mu, Junling Wang, Weizhao Hu*, Lei Song*

*State Key Laboratory of Fire Science, University of Science and Technology of China, 96 Jinzhai Road, Hefei, Anhui 230026, PR China*

## HIGHLIGHTS

- Hierarchical $TiO_2$@LDH@$Ni(OH)_2$ nanospheres with regular-oriented nanocatalyst shells are synthesized.
- $TiO_2$@LDH@$Ni(OH)_2$ improves the mechanical performance of UPR.
- $TiO_2$@LDH@$Ni(OH)_2$ enhances the flame retardancy and toxic smoke suppression of UPR.

## GRAPHICAL ABSTRACT

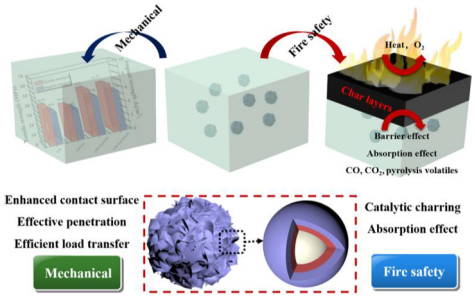


## ARTICLE INFO

*Keywords:*
Hierarchical core–shell architecture
Unsaturated polyester resin
Nanocatalyst
Interfacial interaction
Fire safety

## ABSTRACT

Due to poor interfacial interaction between titanium dioxide ($TiO_2$) and polymers, the fabrication of high-performance polymer/$TiO_2$ composites is still a big challenge. To improve and fully utilize the catalytic efficiency of $TiO_2$ for flame retardant application, in this work, a hierarchical core–shell $TiO_2$-based architecture was constructed, composed by $TiO_2$ nanospheres (core) and oriented-growth Co-Al layered double hydroxide (LDH)@Ni$(OH)_2$ nano-catalyst (shell). As-fabricated hybrids with a fine frame construction improved the interfacial interaction with unsaturated polyester resin (UPR) matrix, contributed by increased contact area and interpenetration between two phases. Through well-contacted interface, the external force can be transferred smoothly to the rigid filler, and thus improved mechanical performance of UPR/$TiO_2$@LDH@$Ni(OH)_2$ nanocomposites. Theoretically, the well-designed structures and optimization of the chemical composition for transition metal compounds are important to effectively reduce fire hazards of UPR composites. Compared with pure UPR, the heat release, flammable pyrolysis products and toxic smoke emission were clearly reduced during the combustion of UPR/$TiO_2$@LDH@$Ni(OH)_2$, which can be attributed to the adsorption effect of core–shell hybrids and the barrier effect of thermostable char layers. Moreover, the total CO release experienced a maximum 53.33% decrease. Herein, this work expands the thinking of the preparation of multifunctional high-performance composites, and designs a novel hierarchical core–shell architecture with multiple regularly oriented shell layers.

* Corresponding authors.
*E-mail addresses:* hwz1988@ustc.edu.cn (W. Hu), leisong@ustc.edu.cn (L. Song).

https://doi.org/10.1016/j.cej.2020.126650
Received 1 April 2020; Received in revised form 8 August 2020; Accepted 10 August 2020
Available online 13 August 2020

## 1. Introduction

The hierarchical core–shell architectures with specific nuclear particles and cladding layers have caused a broad attention, due to the generation of superior physical and chemical properties to the single component, such as optimized chemical composition, increased surface area, favorable thermal stability, excellent optical and magnetic properties, etc [1,2]. Hydrothermal method is commonly used to prepare various components on the surface of nucleation layers, which can not only construct the core–shell hybrids with low thermal stress, few macroscopic defects, high uniformity and high purity, but also make it possible to fabricate novel multifunctional nanocomposites with proper chemical composition and physical structure [3]. The construction of core–shell structures mainly depends on the compatibility and interaction between the shell and the core. The shell can not only improve the surface charge and surface performance of kernel particles, but also facilitate to the stability and dispersion of the kernels [4,5]. Meanwhile, the inner core serves as the template, controlling the morphology and size of as-prepared hierarchical core–shell architectures. Silicon dioxide [6], carbon nanotubes [7], polyphosphazene [8], and ammonium polyphosphate [9] are common core materials in flame retardant fields, which can improve the thermal stabilities, fire safety performance and even mechanical properties of the corresponding polymer composites. It is worth noting that the core–shell nanoparticles containing many different metallic elements have broad application prospects in electronics, biosensor, optics and catalysis, etc [10,11]. Especially, the hierarchical core–shell architectures that consist of transition metal compounds can be effective flame retardants for polymer materials due to their strong catalytic activity and selectivity [12]. When advanced core–shell hybrids are constructed with catalytic metal elements and exhibit the catalytic charring effect during combustion of polymer, they will promote the cyclization, crosslinking and polymerization of pyrolysis products [13].

The core–shell structure with monodispersity, maneuverability and controllability can regulate the properties of the as-fabricated hybrids to a large extent, thus expanding their application fields. Titanium dioxide ($TiO_2$) is widely used in traditional industries such as coatings, artificial fibers, electronic components, ceramics and cosmetics, due to its excellent moisture and gas sensitivity, photocatalysis and dielectric properties [14,15]. Recently, when non-toxic, low-smoke, high-efficiency and halogen-free flame retardant are becoming mainstream of commercial applications, this highly catalytic active, non-toxic, and thermostable nanomaterial is gradually applied to fabricate $TiO_2$-based flame retardants. For example, $TiO_2$ has been incorporated into epoxy [16], polylactic acid [17], poly(vinyl chloride) [18], polycarbonate [19] and other polymers, to prepare high-efficiency flame-retardant polymer composites. However, due to the large specific surface area and surface energy, $TiO_2$ is prone to agglomeration in the application process, resulting in low catalytic efficiency and underutilized performance [20].

Fortunately, its typical structure is also the key to solve these problems. The regular appearance, large specific surface area and abundant surface groups of $TiO_2$ are beneficial to the valence bond connection, thus making it easy to grow appropriate shell layers to construct hierarchical core–shell architectures. Therefore, $TiO_2$ can serve as a preferred core substrate to prepare high-efficiency flame retardants with a regular core–shell structure. Meanwhile, the selection of shell material is a crucial factor for the preparation of multifunctional core–shell flame retardants. It has been found that compounds containing transition metal elements such as cobalt and nickel can be used to fabricate flame-retardant polymer composites, through catalytic charring effect in condensed phase, as well as adsorption removal of toxic smoke during combustion process [21,22]. Therefore, core–shell hybrids containing transition metal compounds, such as $TiO_2$, LDH and $Ni(OH)_2$, can theoretically enhance the fire safety performance of polymer materials [23,24].

However, there are few researches focusing on the construction of multi-layer regularly oriented shell structures on the surface of $TiO_2$ nanospheres. Meanwhile, few works focus on analyzing the effect of hierarchical core–shell $TiO_2$-based architectures with regularly oriented shells on the mechanical properties, flame retardant performance and toxic smoke of unsaturated polyester resin (UPR). UPR is the most commonly used thermosetting resin in fiber- reinforced composite, which is widely used in construction, chemical industry, transportation and electrical, because of its low price, light weight, high tensile strength, high chemical corrosion resistance and insulation [25,26]. However, UPR is highly flammable, and the cross-linked polystyrene chain segment in polymer chains would release a large number of styrene monomers and oligomers during combustion process. These flammable pyrolysis products would burn at temperature above 400℃, releasing lots of heat and harmful smoke, which can increase the fire hazard and greatly limit the wide application of UPR. The growth of regularly oriented transition metal compound on the surface of $TiO_2$ nanospheres can effectively inhibit the agglomeration of nanoparticles and improve the activity and stability of hierarchical core–shell nanocatalysts. The ordered construction of orientated shell layers can act as the bridging materials, which increase the contact surface area and enhance the interfacial interaction between $TiO_2$ and UPR [19]. Due to the strong mechanical interlocking between hierarchical core–shell $TiO_2$-based architectures and matrix, the tensile and impact strengths of composites can be improved. More importantly, the catalytic charring effect and adsorption removal of toxic smoke caused by core–shell nano-catalysts with optimized chemical composition and reasonable core–shell construction, would be an effective method to reduce the fire hazards of UPR composites [27,28].

In this work, considering the poor fire safety and mechanical performance of UPR, a novel high-efficiency core–shell nano flame retardant with regularly oriented shell layers ($TiO_2$@LDH@$Ni(OH)_2$) was successfully synthesized. This hierarchical core–shell architecture was fabricated through the orientated growth of CoAl-LDH on the surface of $TiO_2$ nanospheres followed by the further ordered growth of $Ni(OH)_2$ nanosheets. Detailed measurements were carried out to analyze the effect of as-fabricated hierarchical core–shell architecture on the mechanical properties, flame retardant performance and harmful gas/smoke suppression of UPR composites. Herein, this work expands the thinking of the preparation of multifunctional high-performance composites, and designs a novel hierarchical core–shell architecture with multiple regularly oriented shell layers.

## 2. Experimental section

### 2.1. Materials

Ammonium hydroxide, ethanol, acetonitrile, titanium isopropoxide, $Co(NO_3)_2{\cdot}6H_2O$, $Al(NO_3)_3{\cdot}9H_2O$, $Ni(NO_3)_2{\cdot}6H_2O$, urea, ammonium fluoride, benzoyl peroxide and trisodium citrate dehydrate were obtained from Sinopharm Chemical Reagent Co., Ltd. Unsaturated polyester resin (UPR, named 196) was bought in Hefei Chaoyu Chemical Co., Ltd.

### 2.2. Synthesis of hierarchical $TiO_2$@LDH nanospheres

$TiO_2$ nanospheres were firstly synthesized based on the previous studies [29]. 1.52 g ammonium hydroxide and 3.64 g of deionized water ($H_2O$) were introduced into 500 mL of homogeneous ethanol/acetonitrile (3:2) mixed solution. Under vigorous stirring, 10 mL of titanium isopropoxide were rapidly added into the mixed solution. A milky suspension was obtained with continuous stirring for 6 h, which was then separated by centrifugation and washed with deionized water and ethyl alcohol. $TiO_2$ nanospheres was eventually obtained after being dried at 60 ℃ overnight. The preparation of $TiO_2$@LDH was as follows [30]. $TiO_2$ nanospheres (0.15 g) were firstly added into 15 mL

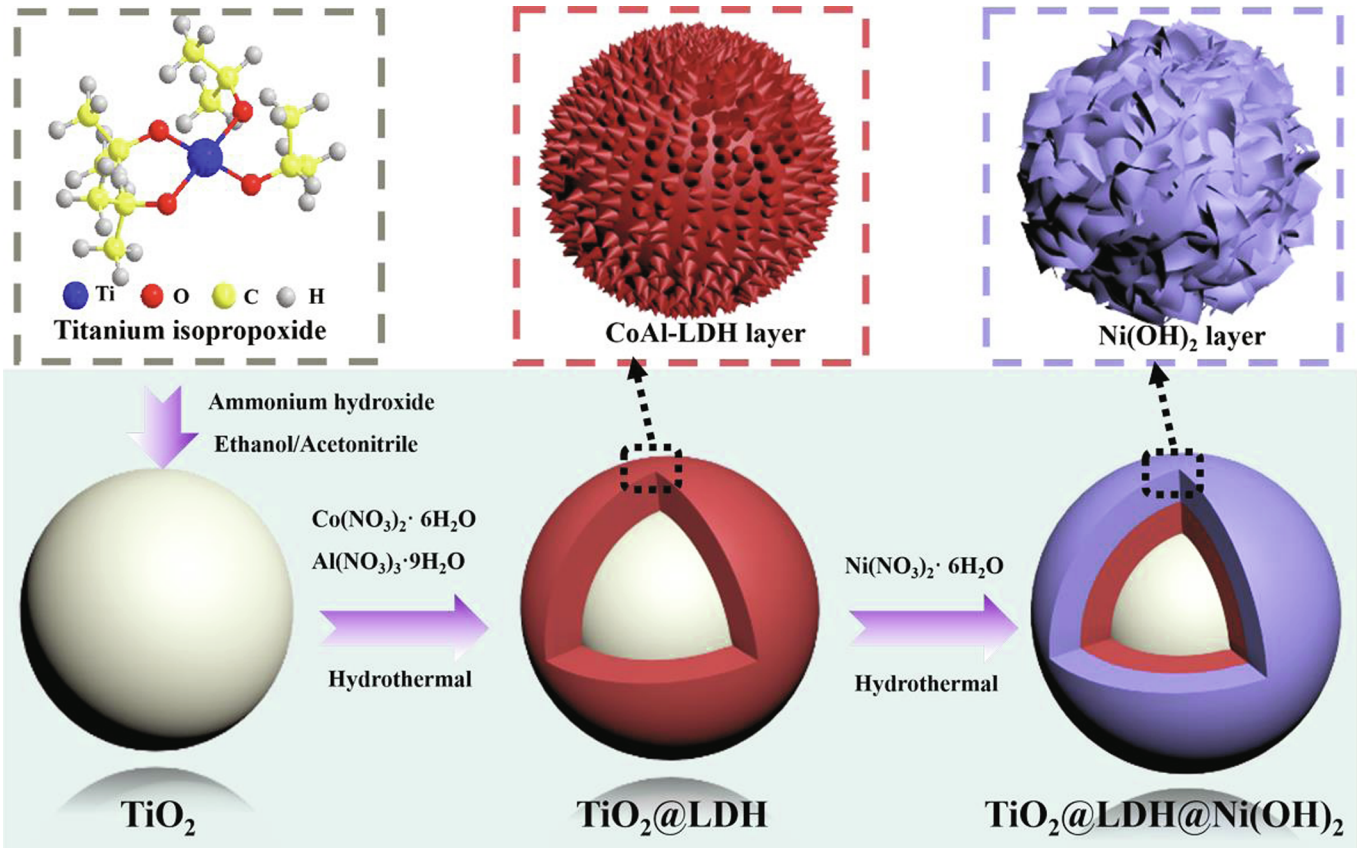


**Scheme 1.** The fabrication process of hierarchical core–shell $TiO_2$@LDH@$Ni(OH)_2$ architecture.

of deionized water and ultrasonic dispersed for 30 min. $Co(NO_3)_2{\cdot}6H_2O$ (0.87 g), $Al(NO_3)_3{\cdot}9H_2O$ (0.38 g), urea (0.60 g) and ammonium fluoride (0.15 g) were evenly dissolved in the above solution. Then, the mixture was poured into a Teflon-lined stainless steel autoclave. After 10 h of hydrothermal reaction at 100 °C, the products were obtained by centrifugation, then washed with deionized water and ethyl alcohol, successively. Finally, the hierarchical $TiO_2$@LDH nanospheres were obtained after drying under at 60 °C overnight.

### 2.3. Synthesis of hierarchical $TiO_2$@LDH@$Ni(OH)_2$ nanospheres

$TiO_2$@LDH (0.1 g) was ultrasonic dispersed into 50 mL of deionized water to get a uniform suspension. After incorporated with Ni $(NO_3)_2{\cdot}6H_2O$ (0.09 g), trisodium citrate dehydrate (0.03 g) and urea (0.03 g), the mixed solution was heated at 100 °C for 7 h of hydrothermal reaction with continuous stirring. The hierarchical $TiO_2$@LDH@$Ni(OH)_2$ nanospheres were collected by centrifugation, washed with deionized water and ethyl alcohol, and finally dried at 60 °C overnight.

### 2.4. Preparation of UPR/$TiO_2$@LDH@$Ni(OH)_2$ nanocomposites

Typically, the $TiO_2$@LDH@$Ni(OH)_2$ nanospheres were incorporated into the UPR matrix, which was then continuously stirred for 4 h under ultra-sonication. Benzoyl peroxide was introduced into the above homogenous mixture as initiator. After ultrasonic agitation for another 1 h, the above mixture was degassed and poured into a mould. The UPR/$TiO_2$@LDH@$Ni(OH)_2$ nanocomposites were obtained after curing at 70 °C for 4 h and then at 120 °C for 3 h. The UPR/$TiO_2$@LDH@Ni $(OH)_2$ nanocomposites were named as UPR/Ti@LDH@$Ni_1$, UPR/Ti@LDH@$Ni_2$ and UPR/Ti@LDH@$Ni_3$ according to various contents of $TiO_2$@LDH@$Ni(OH)_2$ nanospheres (1, 2 and 3 wt%) in UPR. By comparison, UPR/$TiO_2$ and UPR/$TiO_2$@LDH nanocomposites were also fabricated with the 3 wt% of corresponding nanospheres through the same preparation method. Meanwhile, to confirm the advantages of the hierarchical core–shell structures, the UPR/$TiO_2$/LDH/$Ni(OH)_2$ composites were also fabricated, with $TiO_2$, LDH and $Ni(OH)_2$ nanoparticles directly mixed into UPR matrix rather than being combined into hierarchical core–shell structures.

### 2.5. Characterization

The scanning electron microscope (SEM) was used to observe the microstructures of $TiO_2$, $TiO_2$@LDH and $TiO_2$@LDH@$Ni(OH)_2$ (PHILIPS XL30E). Transmission electron microscopy (TEM) was applied to investigate morphologies of nanospheres (JEM-2100F, Japan electron Optics Laboratory Co., Ltd). X-Ray photoelectron spectroscopy (XPS, VG ESCALAB MK-II electron spectrometer, V.G. Scientific Ltd., UK) was used to analyze the chemical composition of nanospheres. The samples for Fourier transform infrared (FTIR, Nicolet 6700 FTIR spectrophotometer) spectra were prepared by mixing KBr powders which were pressed into tablets. The CMT6104 universal testing apparatus was used to measure the tensile strength of UPR composites (sample sizes:100 mm × 10 mm × 3 mm, Shenzhen SANS Material Detection Co., Ltd., China). The ZBC1400-A pendulum was used to carry out the Charpy impact tests for UPR composites (MTS Systems, China). According to the GB/T 1043.1–2008, the sizes of un-notched samples were were 80 mm × 10 mm × 4 mm, and the adopted impact energy was 4 J. SEM was also used to observe fracture surface and microstructures of the char residues for UPR composites (JEOL JSM-6700). According to ISO 5660, the flame retardancy of samples was investigated by cone calorimeter (UK Fire Testing Technology) at a heat flux of 35 $kW{\cdot}m^{-2}$, and dimensions of samples were 100 × 100 × 3 $mm^3$. According to ASTM D3801-1996, the dimensions of specimens for vertical burning test (UL-94, model CFZ-2, Jiangning Analysis Instrument, China) were 130.0 × 13.0 × 3.2 $mm^3$. According

to ASTM D2863-2010, the dimensions of specimens for limiting oxygen index (LOI, HC-2 oxygen index meter) were 100 × 6.5 × 3.0 $mm^3$. Thermogravimetric analysis (TGA, Q5000 thermoanalyzer instrument) was used to investigate the thermal stability of UPR composites at a linear heating rate of 20 ˚C/min from room temperature to 800 ˚C in 50 mL/min of nitrogen. Combined TGA analyzer and FTIR spectrophotometer (TGA-FTIR) was used to analyze the pyrolysis products of UPR composites. The experimental parameters were as follows: sample (5–10 mg), heating rate (20 ℃/min), temperature range (30 to 800 ˚C), atmosphere (30 mL/min of nitrogen).The FTIR (Nicolet 6700 FTIR spectrophotometer) was also used to analyze the condensed phase products of the neat and UPR/Ti@LDH@$Ni_3$ composites heated at different temperatures.

## 3. Results and discussions

### 3.1. Fabrication procedure and mechanism

The fabrication process of hierarchical core–shell $TiO_2$@LDH@Ni$(OH)_2$ architecture was shown in Scheme 1. SEM was used to visually analyze the structures of $TiO_2$, $TiO_2$@LDH and $TiO_2$@LDH@Ni$(OH)_2$ nanospheres. As shown in Fig. 1a and d, $TiO_2$ nanospheres present relatively smooth and homogeneous surface. After 10 h of hydrothermal reaction at 100 ˚C, the surface morphologies of $TiO_2$@LDH nanospheres are more rough, exhibiting unique thorn needle-like architectures (Fig. 1b and e). The growth of CoAl-LDH can be decomposed into two steps. First, metal cation and anion are successively absorbed on $TiO_2$ surface, facilitating the rapid growth and deposition of CoAl-LDH crystal nuclei [31]. Then, the crystal nuclei gradually grow into LDH shells in 10 h of hydrothermal reaction, which are uniformly distributed on the surface of the $TiO_2$ nanospheres. It is worth mentioning that the thorn needle-like morphologies are different from the usual hexagonal LDH nanosheets, because the restricted surface area of $TiO_2$ are not large enough to develop complete hexagonal layer structures. As synthesized LDH shell provides large surface area and reactive sites for the secondary shell. Whereafter, Ni$(OH)_2$ shells grow in specific orientation, interrelated with each other, and form flower-like architecture (Fig. 1c and f). The oriented growth of Ni$(OH)_2$ shells is ascribed to heterogeneous nucleation and oriented growth of Ni$(OH)_2$ on the surface of $TiO_2$@LDH. Ni$(OH)_2$ crystal nuclei were firstly formed from hydroxyl ions and Ni ions during the process, which were then adsorbed on LDH layers through citrate anions. Meanwhile, $NH_3$ in solutions can anchor on the surface of Ni$(OH)_2$ crystal seeds through the hydrogen bonding, which limited the outward growth and facilitated the in-plane crystal growth mode of Ni$(OH)_2$ nanosheets [32]. In addition, particle size distributions of $TiO_2$, $TiO_2$@LDH and $TiO_2$@LDH@Ni$(OH)_2$ were measured, and shown in Fig. 1g-i. When the $TiO_2$ nanospheres are clustered together in the range of 310–330 nm, the diameter distribution of $TiO_2$@LDH are ranging from 380 to 410 nm. Furthermore, after further growth of oriented Ni$(OH)_2$ shells on the surface, the flower-like hierarchical nanospheres show evenly distributed and further increased size distributions, at around 410–440 nm.

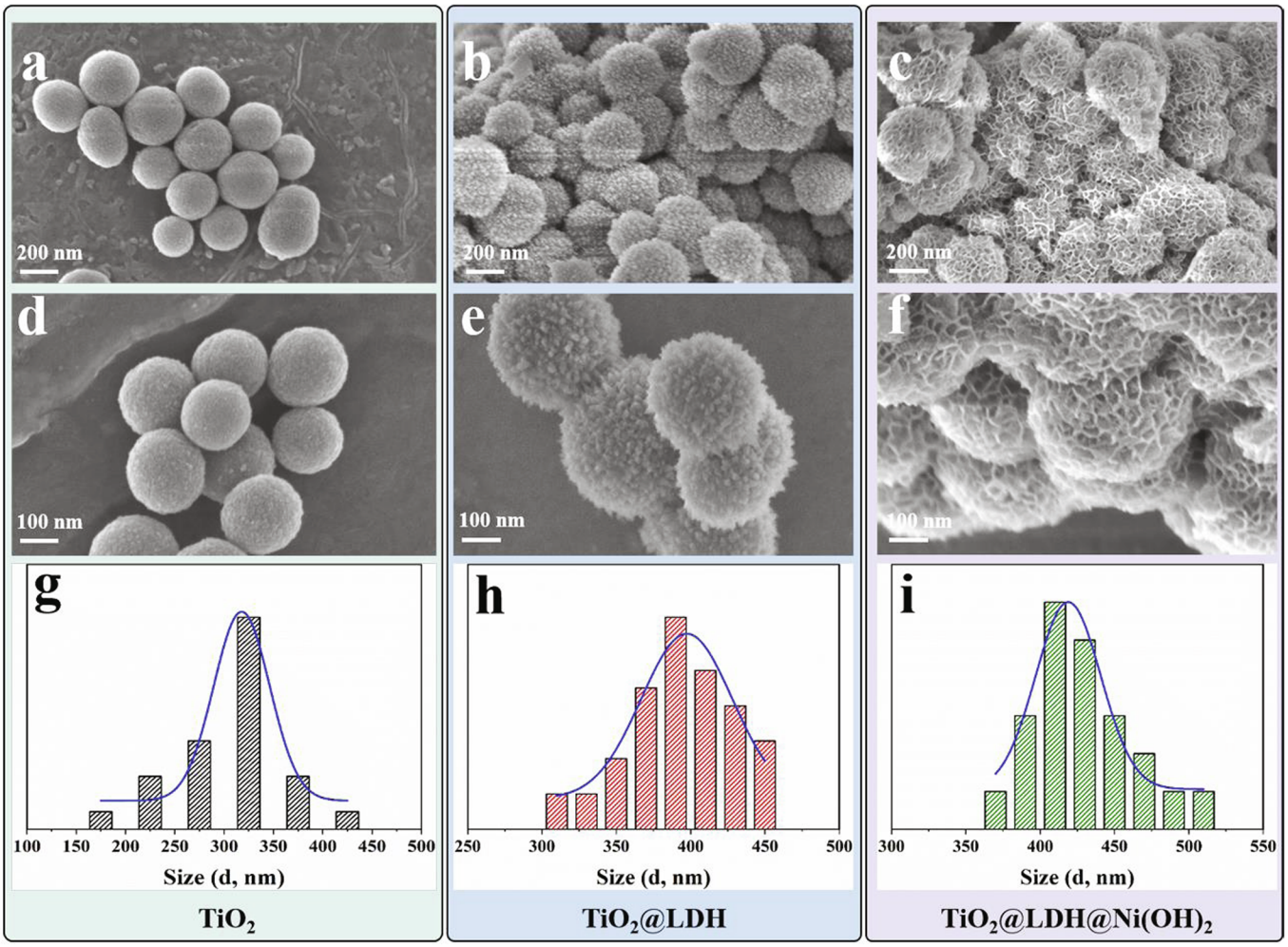


**Fig. 1.** The SEM images and the corresponding particle size distributions for $TiO_2$ (a, d and g), $TiO_2$@LDH (b, e and h) and $TiO_2$@LDH@Ni$(OH)_2$ (c, f and i).

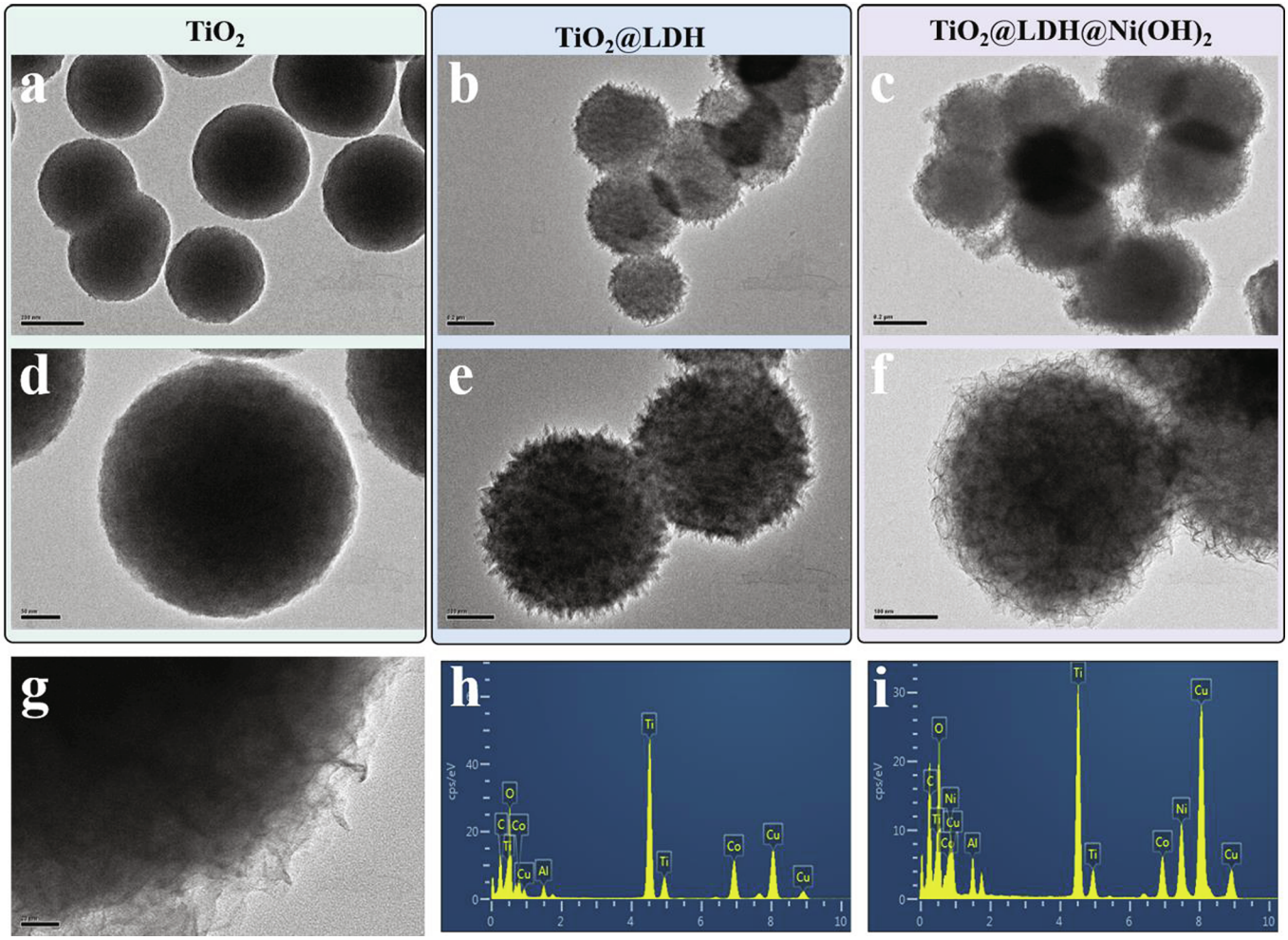


**Fig. 2.** The TEM images for (a, g) $TiO_2$, (b, e) $TiO_2$@LDH and (c, f and g) $TiO_2$@LDH@$Ni(OH)_2$; The EDX results of (h) $TiO_2$@LDH and (i) $TiO_2$@LDH@$Ni(OH)_2$.

### *3.2. Composition analysis of hierarchical $TiO_2$@LDH@$Ni(OH)_2$ nanospheres*

TEM and its EDS results further indicated the successful preparation of hierarchical architectures. Compared with $TiO_2$ nanospheres (Fig. 2a and d), $TiO_2$@LDH clearly exhibit thorn needle-like architectures (Fig. 2b and e). EDS result in Fig. 2h reveal the existence of Co and Al elements. The hierarchical $TiO_2$@LDH@$Ni(OH)_2$ nanospheres show flower-like surface structures, due to successful growth of $Ni(OH)_2$ shells on the surface of $TiO_2$@LDH (Fig. 2c, f and g), which can be also confirmed by its EDS analysis (Fig. 2i). For FTIR spectra in Fig. 3a, the broad characteristic signal at about 3400 $cm^{-1}$ is attributed to stretching vibration of –OH. Compared with neat $TiO_2$, peaks at 575 $cm^{-1}$ and 740 $cm^{-1}$ for $TiO_2$@LDH and $TiO_2$@LDH@$Ni(OH)_2$ are ascribed to Co-O and Al-O stretching vibration, respectively [33]. Furthermore, the peak located at around 660 $cm^{-1}$ in the $TiO_2$@LDH@$Ni(OH)_2$ spectrum is associated with Ni-OH bending vibrations, indicating the successful growth of $Ni(OH)_2$ surface layer in hierarchical architectures [34,35]. XPS was used to identify the element compositions of surface and their valence states. As depicted in Fig. 3b, the curve of $TiO_2$@LDH shows the elements Co, Al, O and Ti. In contrast, the merging Ni element on the spectrum of $TiO_2$@LDH@$Ni(OH)_2$ indicates the presence of $Ni(OH)_2$. Ti 2p1/2 and Ti 2p3/2 peaks at 464.0 and 458.3 eV are detected at high resolution by the Ti 2p curve, where Ti 2p3/2 are deconvoluted into two peaks at 458.2 ($Ti^{3+}$) and 458.7 eV ($Ti^{4+}$), and Ti 2p1/2 are fitted into 463.7 ($Ti^{3+}$) and 464.5 eV ($Ti^{4+}$) curves, respectively (Fig. 3c) [30]. From the spin orbit of Co 2p in Fig. 3d, Co 2p3/2 and Co 2p1/2 at 781.8 and 797.8 eV, and corresponding satellite peaks at 787.1 and 803.5 eV appear. Meanwhile, the Co 2p3/2 and Co 2p1/2 can be divided into the characteristic peaks of $CO_2^{+}$ and $Co^{3+}$ [31]. The O 1 s signal is fitted into three characteristic peaks at 529.9, 531.3 and 532.3 eV, which are ascribed to the metal–oxygen (M − O) bonds, –OH and adsorbed oxygen, respectively (Fig. 3f) [36].

### *3.3. The mechanical performance of UPR composites*

The effect of hierarchical $TiO_2$@LDH@$Ni(OH)_2$ structure on mechanical performance of UPR composites was analyzed through tensile and impact tests. As depicted in Fig. 4, the tensile and impact strengths of UPR/$TiO_2$ are deteriorated, compared with that of neat UPR. However, the addition of hierarchical $TiO_2$@LDH and $TiO_2$@LDH@$Ni(OH)_2$ contribute to the gradual enhancement of tensile and impact strengths of UPR composites. Whereas, the tensile and impact strengths of UPR/$TiO_2$/LDH/$Ni(OH)_2$ are even lower than that of neat UPR. The results indicate hierarchical $TiO_2$@LDH@$Ni(OH)_2$ architectures are more conducive to the improvement of mechanical performance for UPR composites, compared with common structure like $TiO_2$/LDH/$Ni(OH)_2$. The enhanced mechanical performance can be explained from SEM images of fracture surface of UPR composites. For neat UPR, the fracture surface is smooth and flat (Fig. 5a-c). After the incorporation of $TiO_2$ particles into UPR, the composites also present a relatively smooth surface under low magnification, with many small $TiO_2$ grains in the view (Fig. 5d-f). By contrast, the fracture surfaces of UPR/$TiO_2$@LDH

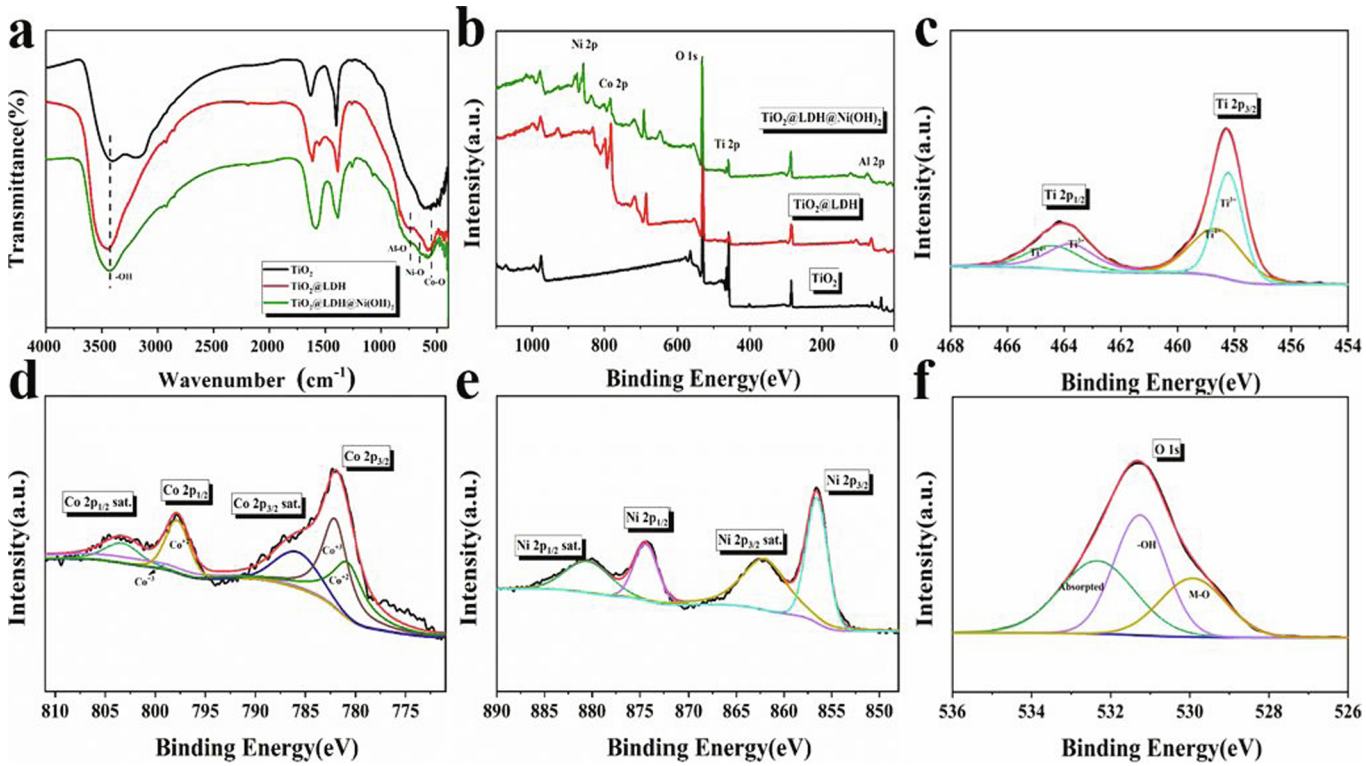


**Fig. 3.** The (a) FTIR and (b) XPS curves of $TiO_2$, $TiO_2$@LDH and $TiO_2$@LDH@$Ni(OH)_2$; The XPS high-resolution spectra for (c) Ti 2p, (d) Co 2p, (e) Ni 2p and (f) O 1 s, respectively.

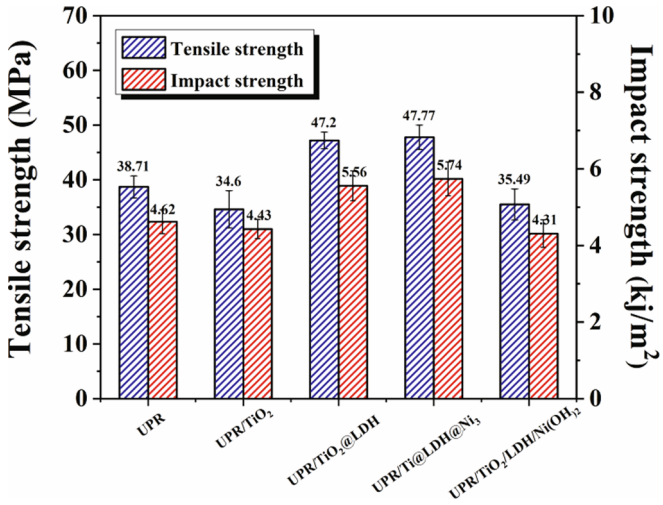


**Fig. 4.** The tensile strengths and impact strengths for UPR composites.

(Fig. 5g-i) and UPR/Ti@LDH@$Ni_3$ (Fig. 5j-l) become significantly rough, with massive plicated wrinkles and fold crimps. Meanwhile, nanoparticles are rarely observed on the surface, because the hierarchical nanospheres are embedded in the matrix. It has been reported that a good interfacial interaction between nanoparticles and matrix is closely linked to the mechanical performances of polymer nanocomposites [37,38]. The oriented growth of LDH and $Ni(OH)_2$ on the surface of $TiO_2$ can increase the surface contact areas between nanoparticles and matrix. Thus, with interpenetration between UPR and orientated-growth LDH and $Ni(OH)_2$ shells, the mechanical locking between nanoparticles and matrix is enhanced, which leads to the plicated cracks and fold crimps on fracture surface. The increased fracture surface area can offer efficient load transfer, thus improving the mechanical performance of UPR composites [39,40].

### 3.4. Flame retardant performance of UPR composites

Heat release rate (HRR) and total heat release (THR) curves were obtained from cone calorimeter. The change of peak heat release rate (PHRR) is shown in Fig. 6a. The incorporation of the as-prepared nanospheres can reduce PHRR values of UPR composites, compared with neat UPR. However, with the same contents, $TiO_2$@LDH@$Ni(OH)_2$ nanospheres bring more prominent decline in PHRR as summarized in Table S1. These results indicate that the flame retardancy of $TiO_2$@LDH@$Ni(OH)_2$ is better than that of $TiO_2$ and $TiO_2$@LDH. A similar tendency can be drawn from THR curves of UPR composites. As shown in Fig. 6b, hierarchical $TiO_2$@LDH@$Ni(OH)_2$ nanospheres are more conducive to lowering the THR values of UPR composites than $TiO_2$ and $TiO_2$@LDH. In comparison with neat UPR, the THR value of UPR/$TiO_2$@LDH@$Ni(OH)_2$ experience 20.45% reduction. For UPR/$TiO_2$/LDH/$Ni(OH)_2$, the PHRR value was slightly lower than that of UPR/Ti@LDH@$Ni_3$. However, the THR value of UPR/$TiO_2$/LDH/$Ni(OH)_2$ was higher than that of UPR/Ti@LDH@$Ni_2$ and UPR/Ti@LDH@$Ni_3$ composites. The UPR/$TiO_2$@LDH@$Ni(OH)_2$ shows the best result as far as THR is concerned whereas UPR/$TiO_2$/LDH/$Ni(OH)_2$ gives the best result in terms of PHRR is attributed to the following reason. As shown in Fig. 6a, in the beginning stage of combustion, the HRR value of UPR/$TiO_2$/LDH/$Ni(OH)_2$ is lower than that of UPR/Ti@LDH@$Ni_3$, because the nano-barrier effects of LDH and $Ni(OH)_2$ nanosheets in UPR/$TiO_2$/LDH/$Ni(OH)_2$ can better inhibit combustion than that of UPR/Ti@LDH@$Ni_3$. Whereas as the combustion continued to 130 s, the HRR value of UPR/$TiO_2$/LDH/$Ni(OH)_2$ is higher than that of UPR/Ti@LDH@$Ni_3$. The decreased HRR of UPR/Ti@LDH@$Ni_3$ is explained by the large surface area of $TiO_2$@LDH@$Ni(OH)_2$ to absorb the combustible products and then promote catalytic charring. The stronger suppression of carbonaceous barrier layers of UPR/Ti@LDH@$Ni_3$ contributes to the best result as far as THR is concerned. All these results confirm that the combination of $TiO_2$, LDH and $Ni(OH)_2$ in hierarchical nanospheres further enhance the flame retardant performance of UPR composites. The results of UL-94 and LOI experiments are listed in

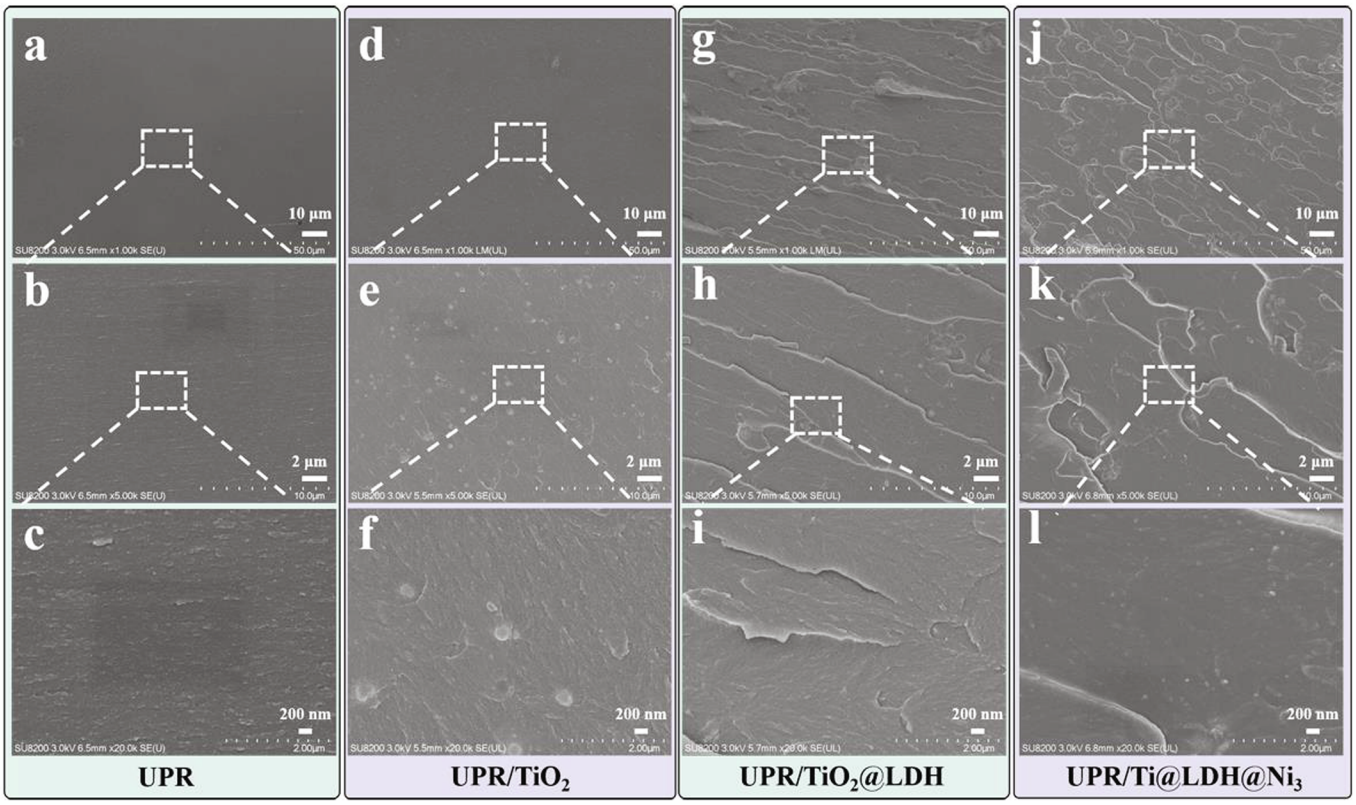


**Fig. 5.** SEM images of fracture surface for (a-c) neat UPR, (d-f) UPR/$TiO_2$, (g-i) UPR/$TiO_2$@LDH and (j-l) UPR/Ti@LDH@$Ni_3$ composites, respectively.

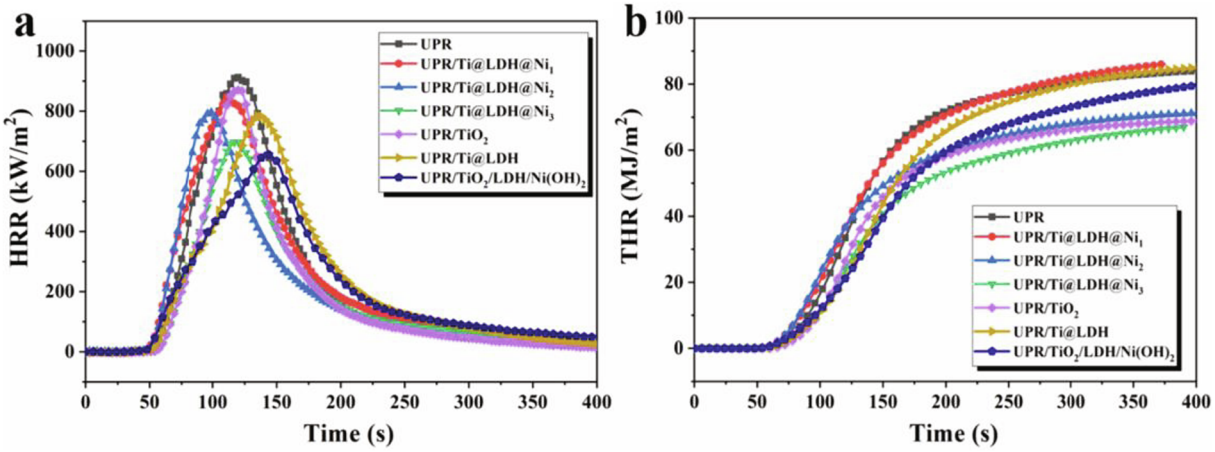


**Fig. 6.** (a) The heat release rate (HRR) and (b) The total heat release (THR) curves for UPR composites.

**Table 1**
The results of UL-94 and LOI.

| Samples | UL-94 | LOI (%) |
|---|---|---|
| UPR | no rating | 20.5 ± 0.5 |
| UPR/$TiO_2$ | no rating | 20.5 ± 0.5 |
| UPR/Ti@LDH | no rating | 21.5 ± 0.5 |
| UPR/Ti@LDH@$Ni_3$ | no rating | 21.5 ± 0.5 |

Table 1. In the UL-94 test, though the UPR composites show no rating, the addition of $TiO_2$@LDH and $TiO_2$@LDH@Ni$(OH)_2$ can slow the flame spread, compared with neat UPR. The LOI value of neat UPR is 20.5, which is similar to the previous literature. However, even with the addition of $TiO_2$@LDH and $TiO_2$@LDH@Ni$(OH)_2$, the LOI values of UPR composites are not effectively increased. The slight increase of LOI values can be ascribed to the low addition of nanospheres.

### 3.5. Toxic smoke analysis

The smoke emission behaviors were assessed through the smoke production rate (SPR) and total smoke production (TSP), which were obtained from cone calorimeter. As presented in Fig. 7a, the hierarchical core − shell $TiO_2$@LDH@Ni$(OH)_2$ nanospheres inhibited the smoke release of UPR composites. With the addition of individual $TiO_2$ in UPR, there was no significant change in the value of peak SPR (PSPR) compared with neat UPR. However, after integrating 3 wt% of hierarchical core − shell $TiO_2$@LDH@Ni$(OH)_2$ nanospheres with UPR, the PSPR value was reduced by 38.46%. Meanwhile, the PSPR value of UPR composites also decreased with the addition of $TiO_2$@LDH nanospheres. However, the decline level was even less than that of the

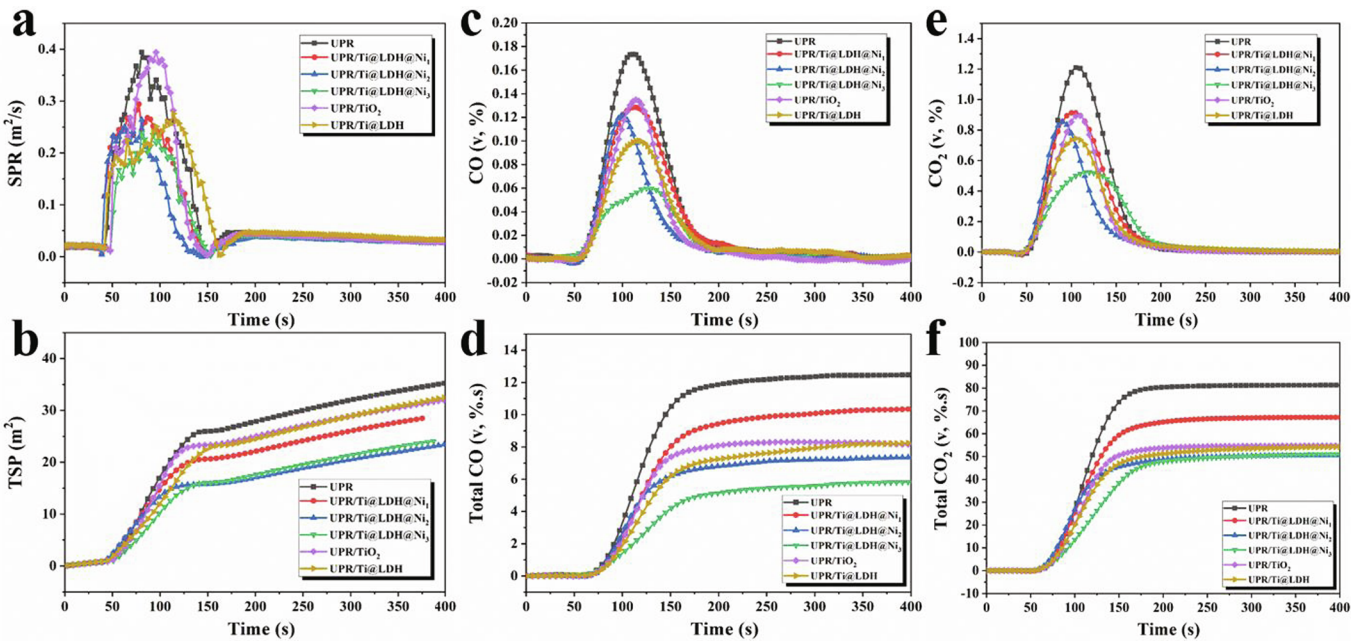


**Fig. 7.** (a, b) Smoke, (c, d) CO and (e, f) $CO_2$ emission behaviors for UPR composites.

corresponding UPR composites with only 2 wt% of $TiO_2$@LDH@Ni$(OH)_2$, indicating the smoke inhibiting effect of $TiO_2$@LDH@Ni$(OH)_2$. Additionally, the TSP values of UPR composites also decreased with the addition of different nanospheres, exhibiting a similar tendency to that of PSPR values (Fig. 7b). UPR/Ti@LDH@$Ni_3$ exhibited a lower PSPR value than that of UPR/$TiO_2$ and UPR/$TiO_2$@LDH. Compared with neat UPR, the TSP value was declined by 31.61% combining 3 wt% of $TiO_2$@LDH@Ni$(OH)_2$ nanospheres and UPR. Among combustion smoke, CO can cause metabolic acidosis and respiratory acidosis for human beings. The release curves of CO and $CO_2$ versus combustion time were obtained from the cone calorimeter. It was found that the incorporation of different nanospheres in UPR exhibited the superior CO and $CO_2$ inhibiting effect, compared with individual UPR. Furthermore, the suppression effect can be increased with the gradual addition of constructed hierarchical architecture. As shown in Fig. 7c, with the same content, $TiO_2$, $TiO_2$@LDH and $TiO_2$@LDH@Ni$(OH)_2$ bring 23.53, 41.18 and 64.11% decreases in the peak values of CO release, respectively. Meanwhile, in contrast to neat UPR, the maximum 53.33% decrease can be obtained for the total CO release with the use of hierarchical $TiO_2$@LDH@Ni$(OH)_2$ nanospheres, indicating their excellent inhibition effect for CO (Fig. 7d). Additionally, more than 57.02 and 30.19% decreases can be obtained for peak value of $CO_2$ and total $CO_2$ release, respectively (Fig. 7e and f). The suppression of toxic smoke greatly reduce the physical and psychological effects of people exposed in fire. Some important parameters are summarized in Table S2.

### 3.6. The thermal behaviors and gaseous pyrolysis volatiles of UPR composites

The thermal stability of UPR composites was evaluated by TGA measurements. TGA and DTG curves are depicted in Fig. 8a and b, and some important data such as the temperatures at 5% and 10% weight loss ($T_{5\%}$ and $T_{10\%}$), temperature at maximum weight loss rate ($T_{max}$) and char residues at 800 ℃ ($Y_c$) are summarized in Table S3. From TGA results, both neat UPR and its nanocomposites experienced one-stage decomposition process. The addition of $TiO_2$, $TiO_2$@LDH and $TiO_2$@LDH@Ni$(OH)_2$ facilitated the decomposition of the corresponding UPR nanocomposites with a slight decrease of $T_{5\%}$, $T_{10\%}$ and $T_{max}$. Furthermore, the addition of nanoparticles, especially hierarchical $TiO_2$@LDH@Ni$(OH)_2$ nanospheres, contributed to the increased thermal stability of materials at a high temperature, producing increased char residues.

TGA-FTIR coupling test was used to further explore the pyrolysis volatiles of neat UPR and UPR/Ti@LDH@$Ni_3$ composites. Several flammable and toxic pyrolysis components can be identified from FTIR spectra, which extracted at maximum evolution rate of pyrolysis volatiles of neat UPR and UPR/Ti@LDH@$Ni_3$ composites. As shown in Fig. 9, neat UPR and UPR/Ti@LDH@$Ni_3$ composites present similar FTIR spectra, where the characteristic peaks at around 2935, 1765 and 1455 $cm^{-1}$ can be attributed to hydrocarbons, carbonyl compounds and aromatic compounds respectively, which severely threaten the life safety in a fire [41]. As shown in Fig. 10a, the total gaseous pyrolysis products of UPR/Ti@LDH@$Ni_3$ composites are decreased compared with neat UPR, indicating the release of flammable and toxic pyrolysis volatiles is reduced. Additionally, some typical pyrolysis volatiles (carbonyl compounds, hydrocarbons and aromatic compounds) experience dramatic decline in the maximum absorbance intensity after incorporating the $TiO_2$@LDH@Ni$(OH)_2$ into UPR matrix, which contributes to the enhancement of fire safety performance for UPR composites (Fig. 10b-d). The reduction of pyrolysis volatiles for UPR/Ti@LDH@$Ni_3$ is attributed to the absorption effect of hierarchical nanospheres and barrier effect of char layers. At the initial stage of thermal degradation, $TiO_2$@LDH@Ni$(OH)_2$ nanoparticles in UPR/Ti@LDH@$Ni_3$ can absorb the organic pyrolysis volatiles because of their large specific surface area. The decreased gaseous pyrolysis products further suppress the smoke generated by the accumulation of hydrocarbons and aromatic compounds. In addition, the reduction of volatiles also helps to reduce the smoke toxicity. Meanwhile, the barrier effect of char layers may cause the decrease of the pyrolysis products.

### 3.7. Condensed phase analysis

FTIR was further applied to analyze the condensed phase of neat UPR and UPR/Ti@LDH@$Ni_3$ composites at different temperatures. In Fig. 11a, several characteristic absorption peaks for neat UPR are seen, such as aromatic ring (1450–1600, 1060–1275, 750 and 700 $cm^{-1}$), C = O (1732 $cm^{-1}$), –$CH_2$ (2955–3060 $cm^{-1}$) and –OH (3444 $cm^{-1}$) [42]. With the temperature increasing, the intensities of characteristic absorption peaks gradually decreased. For example, the peak of –OH was weakened at 250 ℃ and disappeared at 360 ℃, due to the

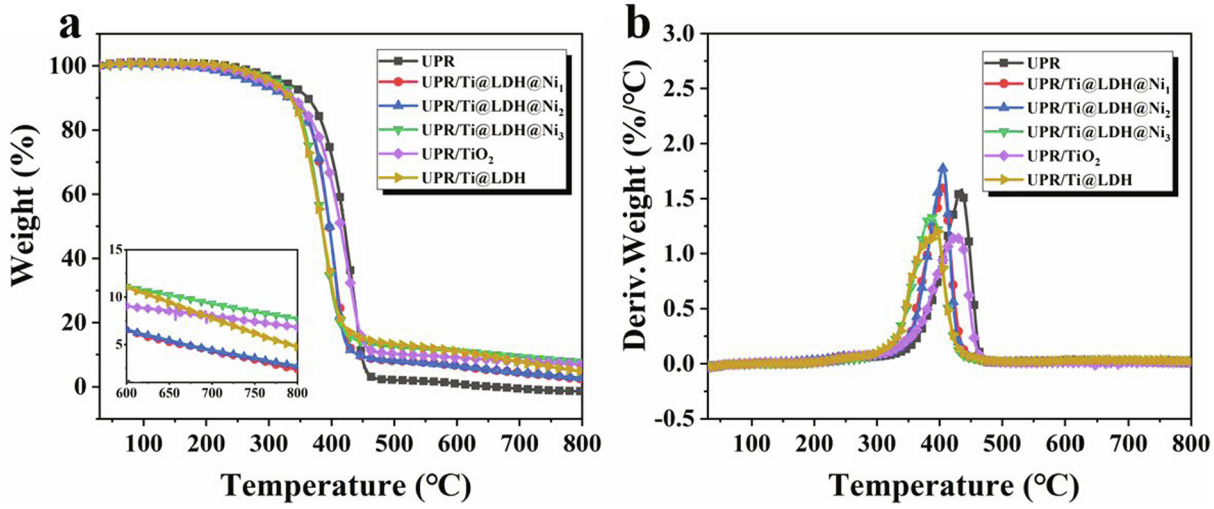


**Fig. 8.** TGA (a) and DTG (b) curves for analysis of thermal stability of UPR composites.

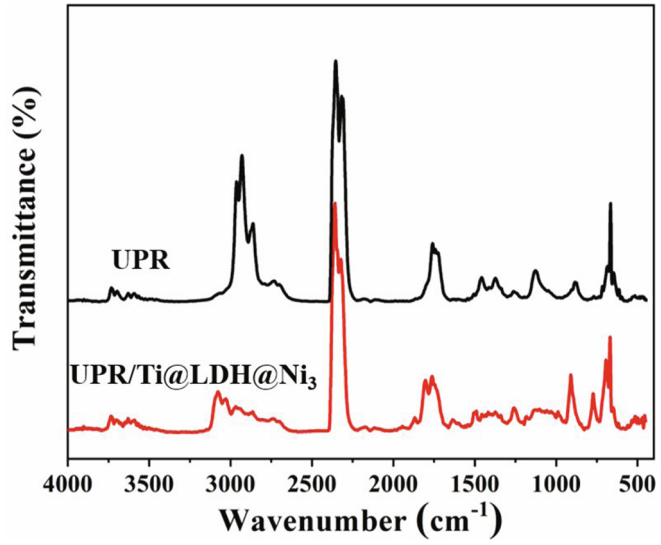


**Fig. 9.** FTIR spectra extracted from process of thermal degradation at maximum evolution rate of pyrolysis volatiles for neat UPR and UPR/Ti@LDH@$Ni_3$ composites.

dehydrating effect during the heating process. Compared with that of neat UPR, the peak intensities for UPR/Ti@LDH@$Ni_3$ composites exhibited some different trends (Fig. 11b). For neat UPR, the relative intensities of absorption bands at 700, 750, 1732 and 2956 $cm^{-1}$ sharply decreased between 360 and 420 ℃, due to the severe thermal degradation of the polyester and polystyrene molecular chains. Whereas, a rapid decline in peak intensities can be observed before 360 ℃ for UPR/Ti@LDH@$Ni_3$, earlier than that of neat UPR. The phenomenon corresponds to TGA results, where the $T_{max}$ of UPR/Ti@LDH@$Ni_3$ was about 50 ℃ lower than that of neat UPR (Figure S1b). Another difference can be observed at 2955–3060 $cm^{-1}$ of C–H stretching, which was used to analyze thermal stabilities of UPR composites during the process of thermal decomposition [43]. The peak intensity of the group also gradually decreased with the rising temperatures. However, at variance with the disappearance of C–H signals at 420 ℃ for neat UPR, the C–H peak still remained in FTIR curves of UPR/Ti@LDH@$Ni_3$, indicating the suppressed pyrolysis process and improved thermal stability of UPR composites at high temperature. This result corresponds to TGA results in Figure S1a, where the retained weight of UPR/Ti@LDH@$Ni_3$ was more than that of neat UPR at around 440 ℃, also indicating the enhanced thermal stabilities at high temperature.

SEM was used to visually observe the morphologies of char residues after combustion in the cone calorimeter. As presented in Fig. 12a and e, many cracks existed on the surface of char residues for neat UPR, and fragmentary char layers cannot restrain the heat transfer from the flame to the polymer, and the release of flammable pyrolysis products to flame zone. For UPR/$TiO_2$ composites, char residues were more compact than that of neat UPR, but some evident holes still existed on the surface, failing to effectively block the transportation of heat and pyrolysis products (Fig. 12b and f). Whereas, for UPR/$TiO_2$@LDH (Fig. 12c and g) and UPR/Ti@LDH@$Ni_3$ (Fig. 12d and h), the integrity of the char layers was improved, where complete and continuous protective barrier layers can be obtained with little cracks and holes on the surface. FTIR was used to analyze char residues of UPR/Ti@LDH@$Ni_3$ after combustion in the cone calorimeter. As shown in Figure S2, the peaks for Ni-O and Co-O appear on the spectrum of UPR/Ti@LDH@$Ni_3$ composites. The chemical compositions of char residues for UPR/Ti@LDH@$Ni_3$ was also investigated by XPS. The high-resolution C, O, Co, Al and Ni elements are detected and the corresponding survey scans are shown in Fig. 13. For C 1 s species, binding energies at 288.7, 286.0 and 284.7 eV can be ascribed to C = O, C-O and C–C signals (Fig. 13a). The O 1 s scan is fitted into three characteristic binding peaks at 532.5, 531.1 and 530.0 eV, where the first two are vibration of C-O and C = O and the last one is M−O (lattice oxygen in metal oxide), indicating generation of metallic oxides in char residues (Fig. 13b). There are four main peaks on the scan curves of high-resolution Co 2p species. The Co 2p1/2 and Co 2p3/2 are at 796.4 and 780.7 eV respectively, and their corresponding satellite peaks are at 803.0 eV and 785.4 eV (Fig. 13c). The characteristic signal at 74.3 eV of Al 2p species in Fig. 13**d** can be assigned to the formation of $Al_2O_3$ during the process of combustion. Furthermore, Ni 2p obit scans of the char residues can be deconvoluted into Ni 2p3/2 and Ni 2p1/2 at 855.5 and 873.3 eV, and their corresponding shakeup satellite peaks are at 861.6 and 880.1 eV, respectively (Fig. 13e).

### *3.8. The mechanism for the improved fire safety performance*

Based on above analysis in gaseous and condensed phases, the improved fire safety of UPR/Ti@LDH@Ni3 is attributed to the absorption effect of hierarchical nanospheres and barrier effect of char layers. $TiO_2$@LDH@Ni$(OH)_2$ nanoparticles in UPR/Ti@LDH@Ni3 can absorb the organic pyrolysis volatiles because of their large specific surface area. Meanwhile, the smoke emission behavior and smoke toxicity are inhibited during the process, due to the reduced release of smoke precursors such as hydrocarbons and aromatic compounds. In addition,

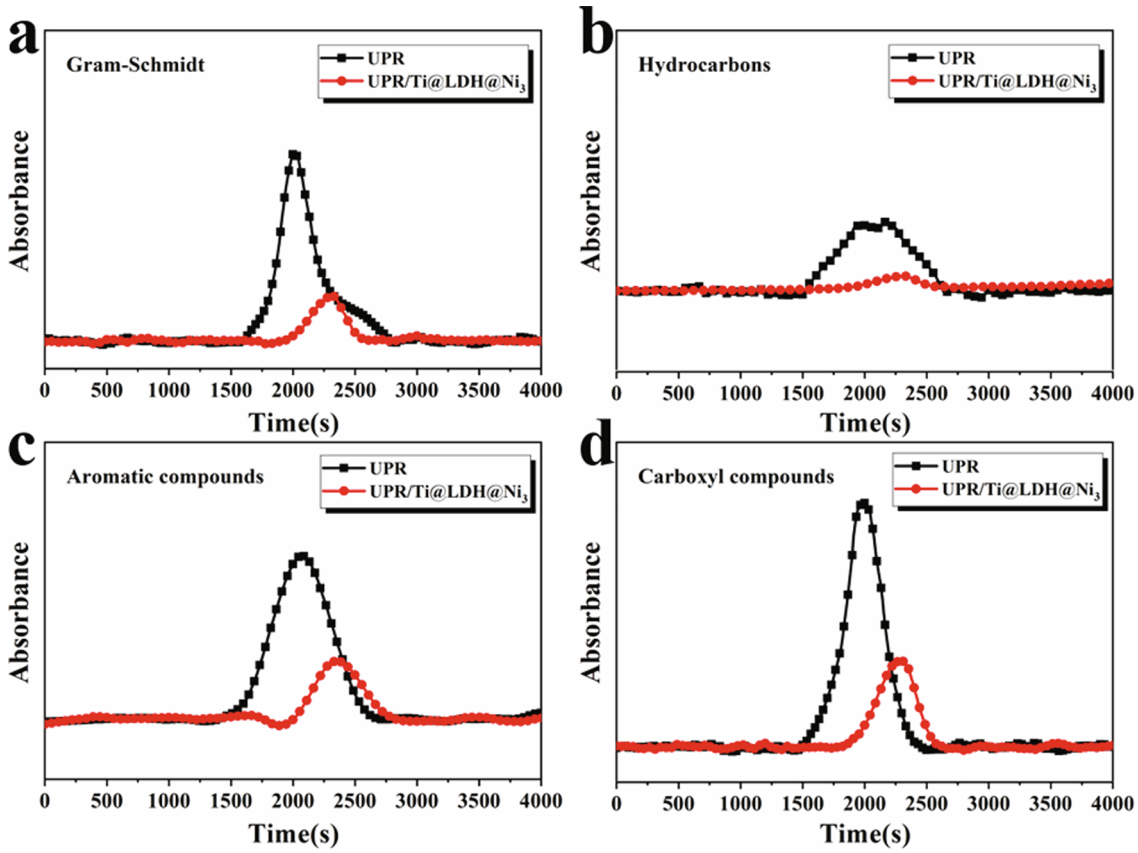


**Fig. 10.** Absorbance intensity curves of Gram-Schmidt (a), hydrocarbons (b), carbonyl compounds (c) and aromatic compounds (d) for neat UPR and UPR/Ti@LDH@$Ni_3$ composites.

during combustion of UPR/Ti@LDH@$Ni_3$ composites, LDH and Ni$(OH)_2$ layers on $TiO_2$ surface would make response to the rising temperature in environment, losing the intercalated ions and interlayer water molecules and producing metal oxides. The superficial nickel oxides firstly promote the formation of carbonaceous layers from UPR matrix, which cover on the surface of metal oxides and serve as a good bridging component between interior metal oxides and exterior matrix [22]. Then, a compact and continuous carbonaceous layers can be obtained through catalytic charring effect, with metal oxides as carbonizing catalyst and reinforcement. Thus, the spread of heat and flammable pyrolysis volatiles can further be restricted with these compact and thermostable protective layers, which effectively limit the development of fire. The decreased release of toxic CO is ascribed to the barrier effect of carbonaceous layers and the absorption of cobalt and nickel containing metal oxides, providing increasing possibility for people escaping from fire. The mechanism for the enhanced fire safety of UPR composites is illustrated as Fig. 14.

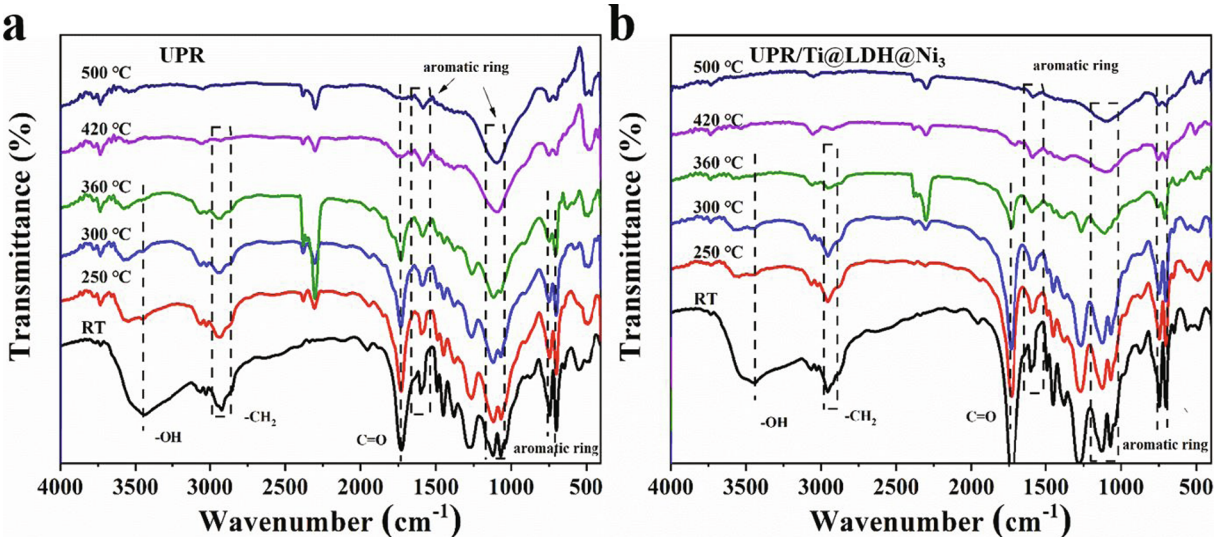


**Fig. 11.** FTIR spectra for (a) neat UPR and (b) UPR/Ti@LDH@$Ni_3$ composites at different temperatures.

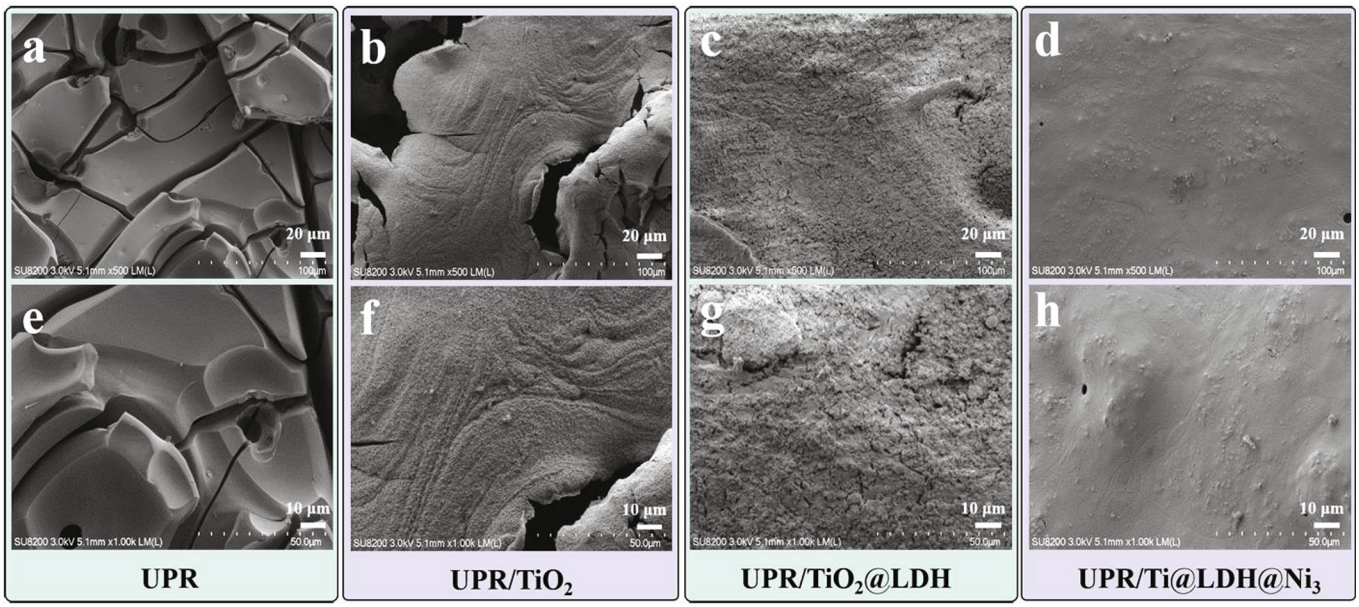


**Fig. 12.** SEM images of char residues for (a, e) neat UPR, (b, f) UPR/$TiO_2$, (c, g) UPR/$TiO_2$@LDH and (d, h) UPR/Ti@LDH@$Ni_3$ composites, respectively.

## 4. Conclusion

In this work, a novel hierarchical core–shell $TiO_2$@LDH@Ni$(OH)_2$ architecture with regularly oriented nano-catalyst shells was successfully prepared through hydrothermal reactions. Then, the corresponding UPR composites were prepared with slightly enhanced mechanical and flame retardant performance as well as toxic gas/smoke suppression. The increased tensile and impact strengths were attributed to improved interfacial interaction between $TiO_2$@LDH@Ni$(OH)_2$ and UPR, which brought enhanced contact surface and efficient load transfer. After the addition of as-fabricated nanospheres, the fire safety performance of UPR composites was improved. Firstly, the parameters about heat release behaviors such as PHRR and THR experienced a slight reduction. The values of PSPR and TSP for UPR/Ti@LDH@$Ni_3$ were reduced by 38.46 and 31.61% respectively, compared with neat UPR. Through the thermal analysis, it was found that some typical flammable and toxic pyrolysis products were inhibited, which is beneficial to the fire control and rescue. Especially, the total CO release experienced a maximum 53.33% decrease. The enhanced fire safety is ascribed to the catalytic charring effect of polymetallic core–shell nanospheres and the barrier effect of resulting thermostable protective layers, as well as the adsorption removal effect of the core–shell nanocatalysts on toxic CO. This work widens the thinking of the preparation of multifunctional high-performance composites, and designs a novel high-efficiency hierarchical core–shell architecture with multiple regularly oriented shell layers.

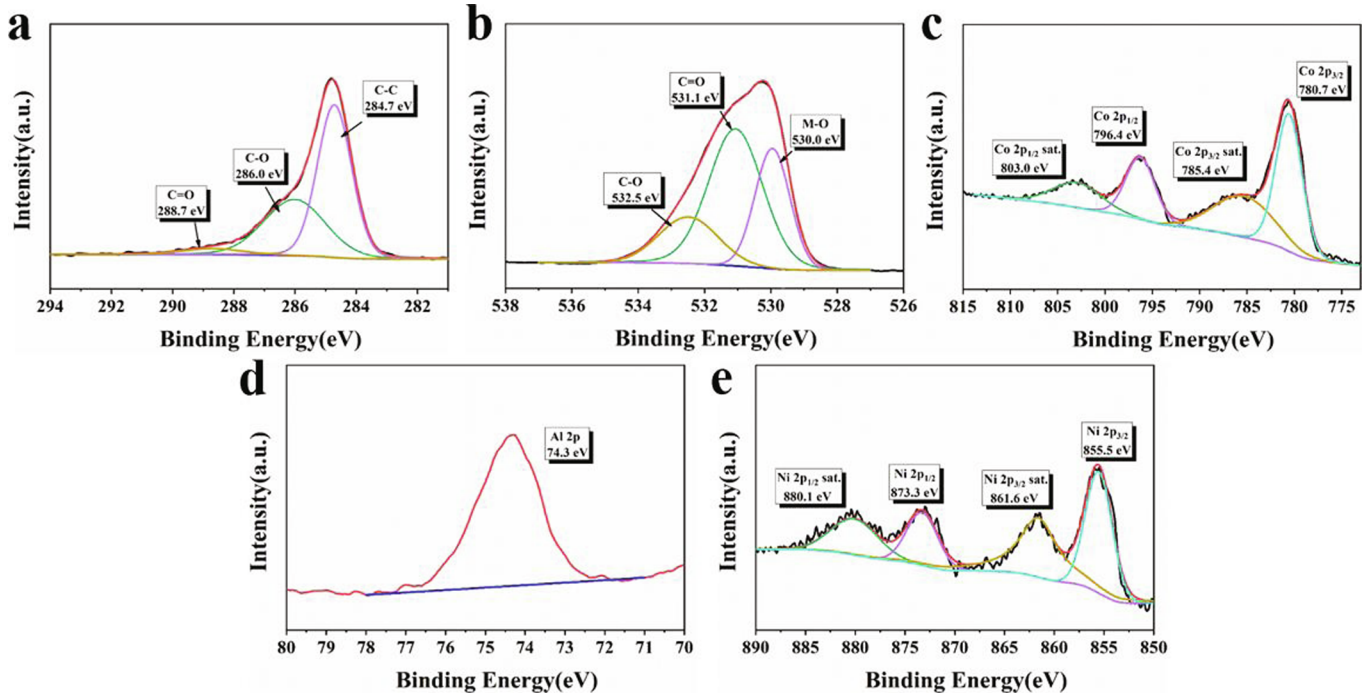


**Fig. 13.** XPS spectra of char residues at high resolution for UPR/Ti@LDH@$Ni_3$ composites: (a) C 1 s, (b) O 1 s, (c) Co 2p, (d) Al 2p and (e) Ni 2p.

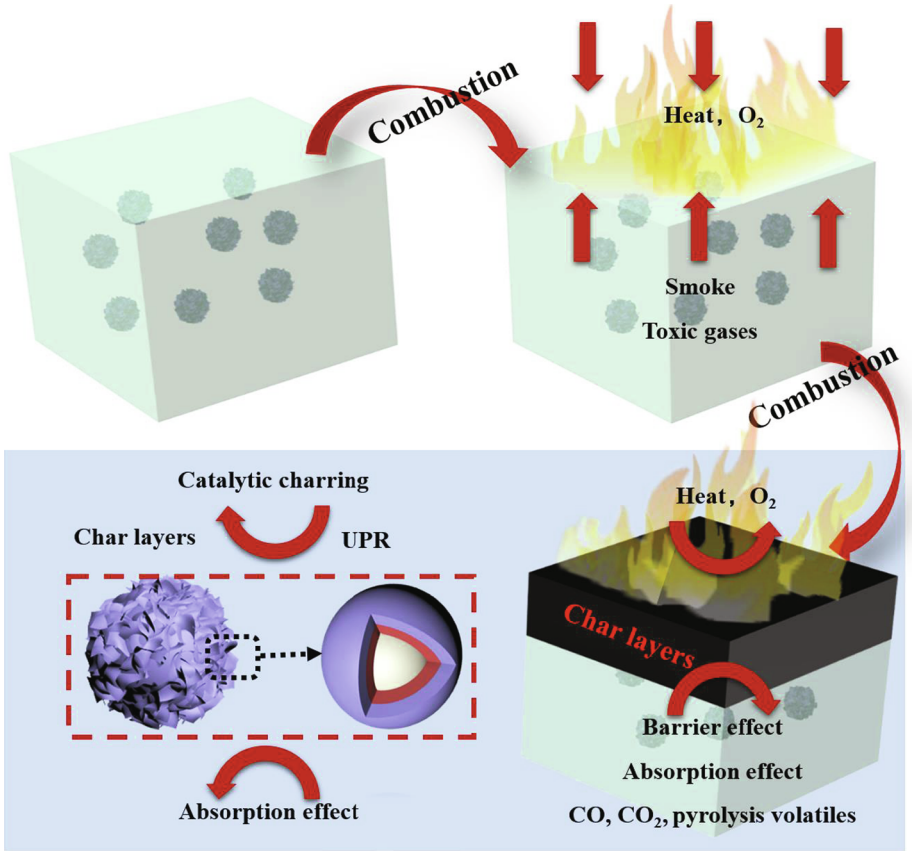


**Fig. 14.** The possible mechanism of the hierarchical core–shell $TiO_2$@LDH@$Ni(OH)_2$ architecture on the improved fire safety performance of UPR composites.

## Declaration of Competing Interest

The authors declare that they have no known competing financial interests or personal relationships that could have appeared to influence the work reported in this paper.

## Acknowledgements

The research was financially supported by the National Natural Science Foundation of China (No. 51991352, No. 51973203 and No. 51874266) and the Fundamental Research Funds for the Central Universities (WK2320000043 and WK2320000044).

## Appendix A. Supplementary data

Supplementary data to this article can be found online at https://doi.org/10.1016/j.cej.2020.126650.

## References

[1] A.M. El-Toni, M.A. Habila, J.P. Labis, Z.A. Alothman, M. Alhoshan, A.A. Elzatahry, F. Zhang, Design, synthesis and applications of core-shell, hollow core, and nanorattle multifunctional nanostructures, Nanoscale 8 (2016) 2510–2531.
[2] A. Meng, L. Zhang, B. Cheng, J. Yu, Dual Cocatalysts in $TiO_2$ Photocatalysis, Adv. Mater. 31 (2019) 1807660.
[3] F. Lu, J. Wang, X. Sun, Z. Chang, 3D hierarchical carbon nanofibers/$TiO_2$@$MoS_2$ core-shell heterostructures by electrospinning, hydrothermal and in-situ growth for flexible electrode materials, Mater. Des. 189 (2020) 108503.
[4] H. Hu, Y. Lin, Y.H. Hu, Synthesis, structures and applications of single component core-shell structured $TiO_2$: A review, Chem. Eng. J. 375 (2019) 122029.
[5] W. Li, A. Elzatahry, D. Aldhayan, D. Zhao, Core-shell structured titanium dioxide nanomaterials for solar energy utilization, Chem. Soc. Rev. 47 (2018) 8203–8237.
[6] Y. Sui, L. Qu, X. Dai, P. Li, J. Zhang, S. Luo, C. Zhang, A green self-assembled organic supermolecule as an effective flame retardant for epoxy resin, Rsc Adv. 10 (2020) 12492–12503.
[7] J. Si, P. Ping, H. Xie, W. Yang, H. Lu, The influence of multiwalled carbon nanotubes-NiCoAl layered double hydroxide hybrids on fire safety performance of poly(ethylene-co-vinyl acetate) composites, Polym. Compos. 39 (2018) E835–E841.
[8] C. Zhang, X. Guo, S. Ma, X. Liu, J. Xu, H. Ma, Synthesis of an organic-inorganic hybrid strontium hydroxystannate nanorod and application as novel flame retardant, Mater. Lett. 229 (2018) 297–300.
[9] X. Jin, S. Cui, S. Sun, X. Gu, H. Li, X. Liu, W. Tang, J. Sun, S. Bourbigot, S. Zhang, The preparation of a bio-polyelectrolytes based core-shell structure and its application in flame retardant polylactic acid composites, Compos. Part A 124 (2019) 105485.
[10] X. He, R. Li, J. Liu, Q. Liu, R. Chen, D. Song, J. Wang, Hierarchical $FeCo_2O_4$@NiCo layered double hydroxide core/shell nanowires for high performance flexible all-solid-state asymmetric supercapacitors, Chem. Eng. J. 334 (2018) 1573–1583.
[11] Y. Pan, K. Sun, S. Liu, X. Cao, K. Wu, W.-C. Cheong, Z. Chen, Y. Wang, Y. Li, Y. Liu, D. Wang, Q. Peng, C. Chen, Y. Li, Core-Shell ZIF-8@ZIF-67-Derived CoP Nanoparticle-Embedded N-Doped Carbon Nanotube Hollow Polyhedron for Efficient Overall Water Splitting, J. Am. Chem. Soc. 140 (2018) 2610–2618.
[12] Y. Zhao, Z. Zhou, G. Chen, Q. Li, In situ synthesis of core-shell ZIF-8@modified sepiolite hybrids for multi-scale construction of epoxy composites with improved low-dielectric properties and thermal stability, J. Mater. Sci-Mater. El. 31 (2020) 6866–6874.
[13] C. Peng, T. Chen, B. Zeng, G. Chen, C. Yuan, Y. Xu, L. Dai, Anderson-type polyoxometalate-based hybrid with high flame retardant efficiency for the preparation of multifunctional epoxy resin nanocomposites, Compos. Part B 186 (2020) 107780.
[14] Y. Ding, I.S. Yang, Z. Li, X. Xia, W.I. Lee, S. Dai, D.W. Bahnemann, J.H. Pan, Nanoporous $TiO_2$ spheres with tailored textural properties: Controllable synthesis, formation mechanism, and photochemical applications, Prog. Mater. Sci. 109 (2020) 100620.
[15] Y. Wang, M. Zu, X. Zhou, H. Lin, F. Peng, S. Zhang, Designing efficient $TiO_2$-based photoelectrocatalysis systems for chemical engineering and sensing, Chem. Eng. J. 381 (2020) 122605.
[16] H. Aziz, F. Ahmad, Effects from nano-titanium oxide on the thermal resistance of an intumescent fire retardant coating for structural applications, Prog. Org. Coat. 101 (2016) 431–439.
[17] W. Wu, T. Liu, D. Zhang, Q. Sun, K. Cao, J. Zha, Y. Lu, B. Wang, X. Cao, Y. Feng, V.A.L. Roy, R.K.Y. Li, Significantly improved dielectric properties of polylactide nanocomposites via $TiO_2$ decorated carbon nanotubes, Compos. Part A 127 (2019) 105650.
[18] B.K. Deka, T.K. Maji, Effect of TiO2 and nanoclay on the properties of wood polymer nanocomposite, Compos. Part A 42 (2011) 2117–2125.
[19] Y.-X. Wei, C. Deng, H. Chen, L. Wan, W.-C. Wei, Y.-Z. Wang, Novel core-shell hybrid nanosphere towards the mechanical enhancement and fire retardance of polycarbonate, ACS Appl. Mater. Interfaces 10 (2018) 28036–28050.

[20] Y.Q. Zheng, Y.F. Yuan, Z.W. Tong, H. Yin, S.M. Yin, S.Y. Guo, Watermelon-like $TiO_2$ nanoparticles (P25)@microporous amorphous carbon sphere with excellent rate capability and cycling performance for lithium ion batteries, Nanotechnology 215407 (2020).
[21] Z. Zhang, J. Qin, W. Zhang, Y.-T. Pan, D.-Y. Wang, R. Yang, Synthesis of a novel dual layered double hydroxide hybrid nanomaterial and its application in epoxy nanocomposites, Chem. Eng. J. 381 (2020) 122777.
[22] Z. Li, J. Zhang, F. Dufosse, D.-Y. Wang, Ultrafine nickel nanocatalyst-engineering of an organic layered double hydroxide towards a super-efficient fire-safe epoxy resin via interfacial catalysis, J. Mater. Chem. A 6 (2018) 8488–8498.
[23] B. Yuan, Y. Hu, X. Chen, Y. Shi, Y. Niu, Y. Zhang, S. He, H. Dai, Dual modification of graphene by polymeric flame retardant and Ni (OH)(2) nanosheets for improving flame retardancy of polypropylene, Compos. Part A 100 (2017) 106–117.
[24] Z. Li, Z. Liu, J. Zhang, C. Fu, U. Wagenknecht, D.-Y. Wang, Bio-based layered double hydroxide nanocarrier toward fire-retardant epoxy resin with efficiently improved smoke suppression, Chemical Engineering Journal 378 (2019) 122046.
[25] P. Penczek, Z. Boncza-Tomaszewski, Unsaturated polyester resins on the verge of the 21st century, Polimery 44 (1999) 709–715.
[26] E.D. Weil, S.V. Levchik, Commercial flame retardancy of unsaturated polyester and vinyl resins: Review, J. Fire Sci. 22 (2004) 293–303.
[27] Z. Chen, T. Chen, Y. Yu, Q. Zhang, Z. Chen, J. Jiang, Metal-organic framework MIL-53 (Fe)@C/graphite carbon nitride hybrids with enhanced thermal stability, flame retardancy, and smoke suppression for unsaturated polyester resin, Polym. Adv. Technol. 30 (2019) 2458–2467.
[28] X.-L. Qi, D.-D. Zhou, J. Zhang, S. Hu, M. Haranczyk, D.-Y. Wang, Simultaneous improvement of mechanical and fire-safety properties of polymer composites with phosphonate-loaded MOF additives, ACS Appl. Mater. Interfaces 11 (2019) 20325–20332.
[29] J.H. Pan, X.Z. Wang, Q. Huang, C. Shen, Z.Y. Koh, Q. Wang, A. Engel, D.W. Bahnemann, Large-scale Synthesis of Urchin-like Mesoporous $TiO_2$ Hollow Spheres by Targeted Etching and Their Photoelectrochemical Properties, Adv. Funct. Mater. 24 (2014) 95–104.
[30] A. Ziarati, A. Badiei, R. Grillo, T. Burgi, 3D Yolk@Shell $TiO_2$-x/LDH architecture: tailored structure for visible light $CO_2$ conversion, ACS Appl. Mater. Interfaces 11 (2019) 5903–5910.
[31] C. Jing, Y. Huang, L. Xia, Y. Chen, X. Wang, X. Liu, B. Dong, F. Dong, S. Li, Y. Zhang, Growth of cobalt-aluminum layered double hydroxide nanosheets on graphene oxide towards high performance supercapacitors: The important role of layer structure, Appl. Surf. Sci. 496 (2019) 143700.
[32] T. Liu, L. Zhang, B. Cheng, W. You, J. Yu, Fabrication of a hierarchical NiO/C hollow sphere composite and its enhanced supercapacitor performance, Chem. Commun. 54 (2018) 3731–3734.
[33] C. Jing, X. Liu, H. Yao, P. Yan, G. Zhao, X. Bai, B. Dong, F. Dong, S. Li, Y. Zhang, Phase and morphology evolution of CoAl LDH nanosheets towards advanced supercapacitor applications, Crystengcomm 21 (2019) 4934–4942.
[34] A. Meng, S. Wu, B. Cheng, J. Yu, J. Xu, Hierarchical TiO2/Ni(OH)(2) composite fibers with enhanced photocatalytic $CO_2$ reduction performance, J. Mater. Chem. A 6 (2018) 4729–4736.
[35] W.L. Ong, S.W.L. Ng, C. Zhang, M. Hong, G.W. Ho, 2D hydrated layered Ni(OH)(2) structure with hollow $TiO_2$ nanocomposite directed chromogenic and catalysis capabilities, J. Mater. Chem. A 4 (2016) 13307–13315.
[36] X. Wei, Y. Zhang, H. He, D. Gao, J. Hu, H. Peng, L. Peng, S. Xiao, P. Xiao, Carbon-incorporated NiO/Co3O4 concave surface microcubes derived from a MOF precursor for overall water splitting, Chem. Commun. 55 (2019) 6515–6518.
[37] M. Bakir, J.L. Meyer, A. Sutrisno, J. Economy, I. Jasiuk, Aromatic thermosetting copolyester bionanocomposites as reconfigurable bone substitute materials: Interfacial interactions between reinforcement particles and polymer network, Sci. Rep. 8 (2018) 1–11.
[38] H. Essabir, M. Raji, S.A. Laaziz, D. Rodrique, R. Bouhfid, A.e.K. Qaiss, Thermo-mechanical performances of polypropylene biocomposites based on untreated, treated and compatibilized spent coffee grounds, Compos. Part B 149 (2018) 1-11.
[39] X. Chen, J. Tao, J. Yi, Y. Liu, R. Bao, C. Li, S. Tan, X. You, Enhancing the strength of carbon nanotubes reinforced copper matrix composites by optimizing the interface structure and dispersion uniformity, Diamond Relat. Mater. 88 (2018) 74–84.
[40] W. Zhou, B. Wang, Y. Zheng, Y. Zhu, J. Wang, N. Qi, Effect of surface decoration of CNTs on the interfacial interaction and microstructure of Epoxy/MWNT nanocomposites, Chemphyschem 9 (2008) 1046–1052.
[41] F. Chu, D. Zhang, Y. Hou, S. Qiu, J. Wang, W. Hu, L. Song, Construction of hierarchical natural fabric surface structure based on two-dimensional boron nitride nanosheets and its application for preparing biobased toughened unsaturated polyester resin composites, ACS Appl. Mater. Interfaces 10 (2018) 40168–40179.
[42] D. Zhao, J. Wang, X.-L. Wang, Y.-Z. Wang, Highly thermostable and durably flame-retardant unsaturated polyester modified by a novel polymeric flame retardant containing Schiff base and spirocyclic structures, Chem. Eng. J. 344 (2018) 419–430.
[43] Y. Hou, W. Hu, Z. Gui, Y. Hu, Effect of cuprous oxide with different sizes on thermal and combustion behaviors of unsaturated polyester resin, J. Hazard. Mater. 334 (2017) 39–48.